A matrix free, partitioned solution of fluid-structure interaction problems using finite volume and finite element methods

R. Suliman[a,b,*], O.F. Oxtoby[a], A.G. Malan[a,c], S. Kok[b,d]

[a]*Aeronautic Systems, Council for Scientific and Industrial Research, Pretoria 0002, South Africa*
[b]*Department of Mechanical and Aeronautical Engineering, University of Pretoria, Pretoria, 0002, South Africa*
[c]*Department of Mechanical Engineering, University of Cape Town, Cape Town, 7700, South Africa*
[d]*Advanced Mathematical Modelling, Modelling and Digital Science, Council for Scientific and Industrial Research, Pretoria 0002, South Africa*

Abstract

A fully-coupled partitioned finite volume–finite volume and hybrid finite volume–finite element fluid-structure interaction scheme is presented. The fluid domain is modelled as a viscous incompressible isothermal region governed by the Navier-Stokes equations and discretised using an edge-based hybrid-unstructured vertex-centred finite volume methodology. The structure, consisting of a homogeneous isotropic elastic solid undergoing large, non-linear deformations, is discretised using either an elemental/nodal-strain finite volume approach or isoparametric Q8 finite elements and is solved using a matrix-free dual-timestepping approach. Coupling is on the solver sub-iteration level leading to a tighter coupling than if the subdomains are converged separately. The solver is parallelised for distributed-memory systems using METIS for domain-decomposition and MPI for inter-domain communication. The developed technology is evaluated by application to benchmark problems for strongly-coupled fluid-structure interaction systems. It is demonstrated that the scheme effects full coupling between the fluid and solid domains, whilst furnishing accurate solutions.

Keywords: Fluid-structure interaction, Partitioned solution, Arbitrary Lagrangian Eulerian (ALE), Finite volume methods, Finite element methods, Parallelisation

1. Introduction

While the field of Computational Mechanics has traditionally been dominated by structual and fluid modelling in isolation, many problems of interest are in truth strongly dynamic systems where there is a close coupling between fluid and solid domains. Fluid–Structure Interaction (FSI) modelling is a branch of Computational Mechanics which aims at accurately calculating these effects in a quantitative manner. For

*Correspondence to: Department of Applied Mathematics and Theoretical Physics, University of Cambridge, Wilberforce Road, Cambridge, CB3 0WA, United Kingdom. Email: R.Suliman@damtp.cam.ac.uk

example, in aeroelastic systems, one important phenomenon is non-linear flutter response which has spawned the field of Computational Aeroelastics [1, 2]. Computational Biomechanics is another major area in which complex dynamic structural responses are intimately coupled with fluid flow in cardiac, arterial and respiratory systems [3, 4, 5, 6]. Other examples of such problems include structural loads on ships [7], flow induced vibrations in nuclear power plants [8] and wind response of buildings [9]. Though recent years have seen much research going into the development of FSI modelling technology [10, 11, 12, 13, 14], the efficient and robust modelling of large-scale, strongly-coupled systems which involve complex geometries is still a work in progress. In this paper, we develop and evaluate a fully-coupled, matrix-free methodology as a contribution towards this challenge. This is incorporated into the *Elemental*[1] flow solver developed for multiphysics applications [15].

This work focusses on FSI systems where there are strong interactions between the fluid and structural domains and weakly-coupled methods are, therefore, not considered as they may diverge or result in inaccurate solutions [16, 17, 18, 19]. As a result, recent research in the field has been devoted to developing strongly-coupled modelling technologies. Strongly-coupled methods can be sub-classified into separate or partitioned and single or monolithic solution methods. The advantage of a monolithic over a partitioned approach is that all the equations are considered simultaneously and a single system of equations is solved, which ensures stability and convergence. However, this approach may suffer from ill conditioning and convergence is generally slow [16]. The advantage of a partitioned approach is that it allows the use of two independent solution techniques for the fluid and solid equations in isolation. The drawback of partitioned approaches is that they generally require a separate coupling algorithm or additional outer iterations between the fluid and solid to achieve strong-coupling, which places an additional computational cost on the scheme [16, 20, 21]. The most popular partitioned coupling algorithms use fixed-point iteration methods or interface Newton-Krylov methods [22, 20]. Fixed-point methods generally make use of Gauss-Seidel iterations which are slow to converge and methods to accelerate convergence, including Aitken and steepest descent relaxation and coarse-grid preconditioning, have been used [22, 19, 23, 24, 21]. The Newton-Raphson methods require the computation of Jacobians, which may be difficult to compute exactly and various methods have been developed that use approximate Jacobians [25, 26, 27].

For the purpose of this work the fluid and structural domains are to be solved in a strongly-coupled partitioned manner, where the transfer of information occurs at solver sub-iteration level leading to a tighter coupling than if the subdomains are converged separately and negating the need for a separate coupling algorithm. This leads to a fully-converged solution at each timestep where both dynamic and kinematic continuity – i.e. continuity of forces and velocities – are satisfied at the fluid/solid interface. Our approach allows independence with respect to spatial discretisation of the fluid and solid domains. Many recent FSI efforts have made use of a single discretisation

[1] *Elemental* referred to in this paper was a scientific toolbox founded by A.G. Malan and has been deprecated in its entirety. A new Elemental^{TM} has since been developed at Univ. of Cape Town which is being commercialised by Elemental Numerics (Pty) Ltd.

scheme, either finite volume [28, 17, 29, 30] or finite element [16, 18, 31, 32, 33, 34], to solve the entire domain, which simplifies the treatment at the interface of the fluid and solid domain. However, each method contains certain inherent advantages and should be used as such. In this work we have chosen to use the finite volume method for the fluid domain. For the solid domain, we use both the finite element method and an enhanced finite volume method [35, 36]. The enhanced finite volume method is essentially a hybrid between the traditional node-based finite volume method, which suffers from locking with high aspect-ratio elements [35], and the element-based strain method [29], which suffers from odd-even decoupling. The fluid physics is described with the incompressible Navier-Stokes equation written for an Arbitrary Lagrangian Eulerian (ALE) coordinate frame. A total Lagrangian formulation is employed in the case of the solid. This prevents discretisation errors from accumulating over time. Dynamic unstructured fluid mesh movement technology is developed using a simple interpolation method in the interests of computational efficiency and parallisability. For the finite volume method, the non-linear, unified governing equations are spatially discretised via a compact unstructured, edge-based finite volume method whose spatial accuracy is notionally of second order. In the interests of both computational and programming efficiency, the chosen spatial discretisation algorithm should be naturally applicable to any part of a fluid or solid mesh. In the case of the fluid, this is achieved by employing an edge-based compact [37, 38] discretisation methodology, which holds the additional advantage of being computationally considerably more efficient than element-based approaches [39] while being ideally applicable to massively parallel distributed memory machines. For the solid domain, we use both the enhanced finite volume method, which is a hybrid of the traditional node-based approach and the element-based strain method, as well as a higher-order Q8 finite element solver. The coupling of a higher-order finite element formulation for the structure and a linear finite volume formulation for the fluid leads to non-matching nodes at the fluid/solid interface and the transfer of information at these nodes will also be addressed in this paper. Dual-timestepping [40] is employed for the purpose of temporal discretisation.

As noted, the proposed partitioned modelling method allows for complete flexibility in terms of the solution strategy employed for the fluid and solid domains as these contain widely varying characteristic velocities – the fluid may be incompressible while the solid may range from compressible to almost incompressible. In the case of the fluid, the Artificial Compressibility Characteristic Based Split (CBS-AC) algorithm [41, 42, 43] is used. This scheme combines two historically opposing methodologies viz. *pressure based* (pressure projection – PP) proposed by Patankar [44] and the *density based* (artificial-compressibility – AC) method introduced by Chorin [45]. The scheme allows matrix-free solution of compressible as well as incompressible flows, which is of key value to large scale distributed memory computing. In this work the CBS-AC algorithm has been extended to an ALE co-ordinate frame. The solid equations are solved via a Jacobi iterative dual-timestepping scheme which is implemented such as to ensure matrix-free and robust solution. Finally, the modelling technology outlined above is validated by application to problems from the literature. The coupled solver is applied to strongly-coupled large-displacement FSI benchmark problems. Rigorous temporal and mesh independent studies are presented.

The outline of this paper is as follows: in Section 2 we present the govering equa-

tions for fluid and solid domains, then describe the discretisation, numerical solution and coupling algorithm in Section 3. In Section 4 we detail the mesh movement algorithm used, and in Section5 discuss parallelisation of the code. We present numerical applications in Section 6 before concluding in Section 7.

2. Governing equations

The fluid-structure interaction to be modelled consists of a viscous incompressible isothermal fluid domain and homogeneous isotropic elastic solid region. The mechanics of each is described via the appropriate governing equation set, which is detailed in this section. Note that for the purposes of this work, the fluid-boundary mesh is fitted to the deforming solid.

2.1. Fluid equations

The fluid flow is governed by the Navier-Stokes equations. In general, these equations are expressed in an Eulerian or spatial frame of reference, which entails a fixed spatial region with fluid flowing through it. For fluid-structure interaction problems the solid deforms and displaces the fluid domain and the fluid equations are written in a manner which allows a Lagrangian description at the fluid-solid interface interpolating to an Eulerian description at the outer boundaries. For this purpose an arbitrary-Lagrangian-Eulerian (ALE) reference frame is used, which accounts for the motion of the FSI interface. The ALE approach was first described by Hirt et al. [46] and later adopted by many others and is now widely used for FSI applications [47]. A dynamic mesh movement algorithm that deforms the fluid mesh is therefore required and is described later. The deforming-spatial-domain/space-time procedure [48, 49] is another popular method for treating moving boundaries and interfaces, while other formulations that utilise a fixed mesh, including immersed boundary [50] and fictitious domain [51] methods, can also be used to perform FSI simulations.

Assuming a viscous, incompressible and isothermal fluid, the equations governing the fluid flow are given by the continuity and Navier-Stokes equations:

$$\frac{\partial v_i}{\partial x_i} = 0 \tag{1}$$

$$\rho\frac{\partial v_i}{\partial t} + \rho(v_j - v_j^*)\frac{\partial v_i}{\partial x_j} + \frac{\partial p}{\partial x_i} - \frac{\partial \sigma_{ij}}{\partial x_j} - \rho f_i = 0 \tag{2}$$

where ρ, v_i, p, σ_{ij} and f_i are the fluid density, fluid velocity, pressure, stress and body forces respectively, x_i are the fixed Eulerian coordinates and v_j^* is the mesh velocity. The term $(v_j - v_j^*)$ is an ALE convective velocity that results from a difference between the fluid velocity and the mesh velocity. We write the governing equations in weak form over an arbitrary and time-dependent volume $\mathcal{V}(t)$ as

$$\frac{\partial}{\partial t}\int_{\mathcal{V}(t)} \mathbf{W} d\mathcal{V} + \int_{\mathcal{S}(t)} \left(\mathbf{F}^j + \mathbf{H}^j - \mathbf{G}^j\right) n_j d\mathcal{S} = \int_{\mathcal{V}(t)} \mathbf{Q} d\mathcal{V}, \tag{3}$$

where

$$\mathbf{W} = \begin{pmatrix} W_0 \\ W_1 \\ W_2 \end{pmatrix} = \begin{pmatrix} \rho \\ \rho v_1 \\ \rho v_2 \end{pmatrix}, \quad \mathbf{H}^j = \begin{pmatrix} 0 \\ p\delta_{1j} \\ p\delta_{2j} \end{pmatrix}, \quad \mathbf{G}^j = \begin{pmatrix} 0 \\ \sigma_{1j} \\ \sigma_{2j} \end{pmatrix}, \tag{4}$$

$$\mathbf{F}^j = \mathbf{W}(v_j - v_j^*), \tag{5}$$

In the above, $\mathcal{S}(t)$ denotes the surface of the volume $\mathcal{V}(t)$, with n_j being the outward pointing unit normal vector; δ_{ij} is the Kronecker delta and $\mathbf{Q}$ is a vector of source terms (e.g. body forces).

To close the fluid governing equations, a constitutive relation for the stress is required. Assuming a Newtonian fluid, the relationship between stress and rate of strain is given by

$$\sigma_{ij} = \mu\Big(\frac{\partial v_i}{\partial x_j} + \frac{\partial v_j}{\partial x_i}\Big), \tag{6}$$

where μ is the fluid viscosity.

2.2. Solid equations

The partial differential equations that describe a homogeneous isotropic elastic solid undergoing large non-linear deformation are given by Cauchy's first equation of motion (balance of linear momentum) [52], which in a total Lagrangian formulation is

$$\int_{\mathcal{V}_o} \Big(\frac{\partial P_{ij}}{\partial X_j} + f_i\Big) d\mathcal{V}_o = \int_{\mathcal{V}_o} \rho_o a_i d\mathcal{V}_o, \tag{7}$$

where P_{ij}, f_i, ρ_o and a_i are the first Piola-Kirchoff stress, body force, density and acceleration, respectively and $\mathcal{V}_o$ is the volume of the solid body in the undeformed configuration.

Assuming an isotropic hyperelastic St-Venant-Kirchoff material model, the constitutive stress-strain relationship is given by

$$S_{ij} = C_{ijkl} E_{ij}, \tag{8}$$

where E_{ij} is the Green-Lagrange strain, S_{ij} is the second Piola-Kirchoff stress and C_{ijkl} is the fourth order elasticity tensor.

The first Piola-Kirchoff stress, P_{ij}, in Eq. (7) is then obtained by multiplying the second Piola-Kirchoff stress, S_{kj}, with the deformation gradient, F_{ik}:

$$P_{ij} = F_{ik} S_{kj}. \tag{9}$$

The deformation gradient relates quantities in the undeformed configuration to their counterparts in the deformed configuration:

$$F_{ik} = \frac{\partial x_i}{\partial X_k} \tag{10}$$

where X_k and x_i are the coordinates of the solid in the undeformed and deformed configurations, respectively.

Finally, to close the governing equations, the relationship between strain and the displacement field is given by

$$E_{ij} = \frac{1}{2}(H_{ij} + H_{ji} + H_{ki}H_{kj}), \tag{11}$$

where H_{ij} is the displacement gradient defined as

$$H_{ij} = \frac{du_i}{dX_j} \tag{12}$$

and u_i is the total displacement of the solid, i.e. $x_i = u_i + X_i$.

3. Discretisation and solution method

3.1. Spatial discretisation

Considering the fluid ALE governing equations (3), all surface integrals are calculated in an edge-wise manner. For this purpose, bounding surface information is similarly stored in an edge-wise manner and termed *edge-coefficients*. The latter for a given internal edge Υ_{mn} connecting nodes m and n, is defined as a function of time as

$$\mathbf{C}_{mn}(t) = \mathbf{n}^{mn_1}\mathcal{S}_{mn_1}(t) + \mathbf{n}^{mn_2}\mathcal{S}_{mn_2}(t) \tag{13}$$

where $\mathcal{S}_{mn_1}$ is a bounding surface-segment intersecting the edge (Figure 1) and the normal unit vectors are similarly a function of time. The discrete form of the surface integral in Eq. (3), computed for the volume surrounding the node m, now follows as

$$\int_{\mathcal{S}_m(t)} \left\{\mathbf{F}^j + \mathbf{H}^j - \mathbf{G}^j\right\} n_j d\mathcal{S} \approx \sum_{\Upsilon_{mn}\cap\mathcal{V}_m(t)} \left\{\overline{\mathbf{F}^j}_{mn} + \overline{\mathbf{H}^j}_{mn} - \overline{\mathbf{G}^j}_{mn}\right\} C^j_{mn} \tag{14}$$

where all $\overline{\bullet}_{mn}$ quantities denote edge-averaged values which are calculated such that second-order accuracy of the overall scheme is ensured [37]. In the case of the fluid, $\overline{\mathbf{G}^j}_{mn} = \left[\overline{\mathbf{G}^j}_{mn}\Big|_{tang} + \overline{\mathbf{G}^j}_{mn}\Big|_{norm}\right]$, where $\mathbf{G}^j\big|_{tang}$ is calculated by employing directional derivatives and $\mathbf{G}^j\big|_{norm}$ is approximated by employing the standard finite volume first derivative terms.

When considering the solid governing equation, Eq. (7), both the finite volume and finite element methods of discretisation are used. For the finite volume method, Eq. (7) is written in weak form as

$$\frac{\partial}{\partial t}\int_{\mathcal{V}_0} \rho_0 v_i d\mathcal{V} = \int_{\mathcal{S}_0} P_{ij} n_j d\mathcal{S} + \int_{\mathcal{V}_0} Q_i d\mathcal{V}, \tag{15}$$

where v_i is the solid velocity and Q_i a vector of source terms. The above method of discretising the stress term would enforce continuous gradients at nodes and element boundaries. To remedy this we consider the element-based-strain approach of Xia and Lin [29], and utilise a hybrid technique. Here, strains E_{11} and E_{22} are evaluated at nodes and averaged to obtain face values (as per the above), whereas E_{12} is evaluated

at the element centre and averaged with the neighbouring element's value to obtain the value at the shared face. This approach was found to be comparable in accuracy to the cited element-based approach while eliminating odd-even decoupling from the solution.

Next, the standard Galerkin finite element method of discretisation is used for spatial discretisation of the solid governing equations. Assuming the body forces to be negligible, casting Eq. (7) into weak form based on the method of weighted residuals and applying the divergence theorem of Gauss gives the general weak form of the solid mechanics boundary value problem:

$$\int_{\mathcal{A}_t} \mathbf{t}_o^p \cdot \mathbf{w} d\mathcal{A}_o - \int_{\mathcal{V}_o} \mathbf{P} \cdot \nabla_X \mathbf{w} d\mathcal{V}_o - \rho_o \int_{\mathcal{V}_o} \mathbf{w} \cdot \mathbf{a} d\mathcal{V}_o = 0 \tag{16}$$

where $\mathcal{A}_t$ is the boundary surface where the surface traction $\mathbf{t}_o^p$ is prescribed and $\mathbf{w}$ is the weighting field. Instead of solving for all possible set of weighting functions for $\mathbf{w}$ to obtain an exact solution, we consider only a finite set of functions for $\mathbf{w}$. These functions are chosen as piecewise-continuous low-order polynomial functions defined on sub-domains (elements) within the total domain $\mathcal{V}_o$ and are referred to as basis or shape functions $[N]$. The weighting field is now interpolated between nodal weighting values $\{W\}$ using these shape functions, i.e.

$$\mathbf{w} = [N]\{W\}. \tag{17}$$

The primary variable, viz. the displacement field $\mathbf{u}$, is interpolated over an element using the same shape functions (Bubnov-Galerkin method):

$$\mathbf{u} = [N]\{U\}, \tag{18}$$

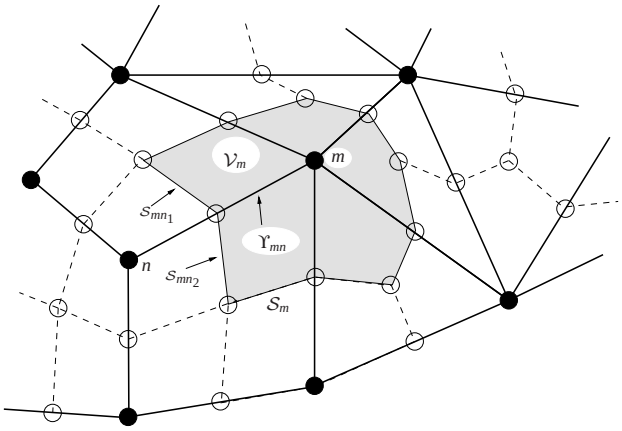

Figure 1: Schematic diagram of the construction of the median dual-mesh on hybrid grids. Here, Υ_{mn} depicts the edge connecting nodes m and n.

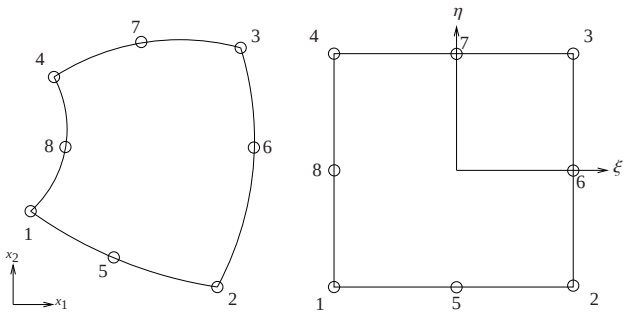

Figure 2: Isoparametric Q8 element in physical space (left) and reference space (right).

where $\{U\}$ is the vector containing the nodal displacements. The domain is discretised into a finite number of non-overlapping control volumes or element domains $\mathcal{V}_e$, which are defined in the undeformed configuration. Simplifying Eq. (16) and expressing it as the sum over all the elements within the domain gives

$$\sum_e \rho_o \int_{\mathcal{V}_e} [N]^T [N] \, d\mathcal{V}_o \{\ddot{U}\} = \sum_e \int_{\mathcal{A}_t^e} [N]^T \{\mathbf{t}_o^p\} d\mathcal{A}_o - \sum_e \int_{\mathcal{V}_e} [B]^T \{P\} d\mathcal{V}_o, \quad (19)$$

where $[B]$ is a matrix containing the derivatives of the shape functions and $\{P\}$ is a vector containing the first Piola-Kirchoff stress.

In this work the solid domain is discretised into eight-noded isoparametric quadrilateral elements. Figure 2 (left) shows an actual Q8 element in physical space and (right) is the reference element mapped or transformed using reference or natural coordinates ξ and η. The integral of the spatial term in Eq. (19) is performed numerically using Gauss quadrature, i.e. the integral is evaluated at a specific number of Gauss points, the result is then multiplied by a weighting factor W_{GP} and the results summed over all the Gauss points. The discrete equation is therefore

$$\sum_e \rho_o \int_{\mathcal{V}_e} [N]^T [N] \, d\mathcal{V}_o \{\ddot{U}\} = \sum_e \{F_{\text{ext}}\} - \sum_e \left(\sum_{\text{Gauss pts}} [B]^T \{P\} \det(\mathbf{J}) W_{GP} \right), \quad (20)$$

where the external loads are simply denoted as $\{F_{\text{ext}}\}$ and $\det(\mathbf{J})$ is the determinant of the Jacobian matrix and is used to transform the integral in the physical coordinates to that in the reference coordinates.

3.2. Geometric conservation

In order for the fluid solution to be as transparent as possible to the movement of the mesh, an identity known as the Geometric Conservation Law (GCL) should be obeyed [53, 54, 55]. It asserts that the momentum flux into a cell due to the motion of the faces should be consistent with the change in momentum of the cell due to its changing volume. That is, the discretised version of

$$\frac{\partial}{\partial t} \int_{\mathcal{V}(t)} d\mathcal{V} = \int_{\mathcal{S}(t)} v_j^* n_j d\mathcal{S}. \quad (21)$$

should hold exactly, which implies that constant spatial fields will be unaffected by arbitrary mesh deformations. The GCL can therefore be said to impose a specific relationship between mesh deformation and the mesh-velocity field. In order for the GCL to hold we could discretise the equation above at node m as

$$\frac{V_m^{t+\Delta t} - V_m^t}{\Delta t} = \sum_{\Upsilon_{mn} \cap \Upsilon V_m(t)} \frac{\delta V_{mn}^t}{\Delta t}, \tag{22}$$

where δV_{mn}^t is the volume swept out by the face lying between nodes m and n between time-steps t and $t + \Delta t$, as in [55], and V_m the volume of the dual-cell containing node m. Alternatively, to second order accuracy

$$\frac{3V_m^{t+\Delta t} - 4V_m^t + V_m^{t-\Delta t}}{2\Delta t} = \sum_{\Upsilon_{mn} \cap \Upsilon V_m(t)} \frac{3\delta V_{mn}^t - \delta V_{mn}^{t-\Delta t}}{2\Delta t}. \tag{23}$$

So, in order for our discretisation to be consistent with the GCL, the mesh velocity flux $\overline{v_j^*} C_{mn}^j$ in the discretisation of (3) is set equal to $(3\delta V_{mn}^t - \delta V_{mn}^{t-\Delta t})/2\Delta t$.

3.3. Temporal discretisation and solution procedure

The solution procedure is to allow for fully coupled solution of all descritised equations while allowing independence in terms of discretisation and solution strategy employed for the fluid and solid domains. We therefore advocate a matrix-free iterative solution process where fluid-solid interface nodes communicate velocities and tractions at each iteration. The resulting solution procedure is detailed below.

For the purpose of transient calculations, a dual-time-stepping temporal discretisation [40] is employed such that second-order temporal accuracy is achieved while ensuring that all equations are iteratively solved simultaneously in an *implicit* fashion.

3.3.1. Fluid

The real-time temporal term is accordingly discretised and added as a source term to the right-hand-side of the discretised fluid equation as

$$Q_i^\tau V^\tau = -\frac{3W_i^\tau V^\tau - 4W_i^t V^t + W_i^{t-\Delta t} V^{t-\Delta t}}{2\Delta t} \tag{24}$$

for $i = 1, 2$ where Δt denotes the real-time-step size, the t superscript is the previous (existing) real time-step and τ denotes the latest known solution to the time-step being solved for viz. $t + \Delta t$.

Considering next the solution procedure, we observe that in the first instance, spatial discretisation of the convective terms via linear interpolation results in destabilising odd-even decoupling. Second, the incompressibility of the fluid results in an overly stiff system. These are circumvented in this work without the loss of notional second-order accuracy via the Artificial Compressibility Characteristic Based Split (CBS-AC) algorithm [41, 42, 43], which has been demonstrated to be robust, efficient and accurate.

To adapt the CBS-AC algorithm to ALE domains we consider Eq. (3) with a time-dependent dual-cell $\mathcal{V}(t)$ which is moving at velocity u_k^*, from which the first incremental solution step written in semi-discrete form follows as:

$$\frac{\Delta W_i^*}{\Delta\tau}V^\tau = -\int_{\mathcal{S}(t)}(F_i^j - G_i^j)n_j dS\Big|^\tau + \int_{\mathcal{S}(t)}\frac{\Delta\tau}{2}(v_k - v_k^*)\frac{\partial}{\partial x_j}(\rho v_i v_j)n_k dS\Big|^\tau + Q_i V|^\tau \quad (25a)$$

for $i = 1, 2$, where the τ superscript denotes the previous (existing) solution or pseudo time-step and $\Delta\tau$ is calculated as in Eq. (32). ΔW_i^* is an auxiliary variable which is used in the second step as:

$$\frac{1}{c_\tau^2}\frac{p^{\tau+\Delta\tau} - p^\tau}{\Delta\tau}V^\tau = -\int_{\mathcal{S}(t)}\left[\rho v_k + \Delta\tau\left(\frac{\Delta W_k^*}{\Delta\tau} - \frac{\partial H_k^j}{\partial x_j}\right)\right]n_k dS\Big|^\tau. \quad (25b)$$

Here c_τ denotes the pseudo-acoustic velocity which is given by

$$c_\tau^2 = \max[\varepsilon^2; 1.2v_j v_j]$$

where ε is typically chosen as $0.1u_{\max}$ where $u_{\max}$ is the peak flow velocity in the domain [40].

The third and final incremental solution step written in semi-discrete form now follows:

$$\frac{W_i^{\tau+\Delta\tau} - W_i^\tau}{\Delta\tau}V^\tau = \frac{\Delta W_i^*}{\Delta\tau}V^\tau - \int_{\mathcal{S}(t)}H_i^j n_j dS\Big|^{\tau+\Delta\tau} \equiv R_i(\mathbf{W}) \quad \text{for } i = 1, 2. \quad (25c)$$

Finally, the fluid mesh velocity v_k^* is calculated via second-order backward difference as follows:

$$v_k^* = \frac{3x_k^\tau - 4x_k^t + x_k^{t-\Delta t}}{2\Delta t} \quad (26)$$

where the nomenclature is as defined previously.

3.3.2. Solid

For the solid equation using the finite volume method, a similar source term is added to the right-hand side of the discretised version of Eq. (15), namely

$$Q_i^\tau V_0 = -\rho_0\frac{3v_i^\tau - 4v_i^t + v_i^{t-\Delta t}}{2\Delta t}V_0 \quad (27)$$

where the nomenclature is as defined previously.

With the finite element method and using the same approach as above, Eq. (19) becomes

$$\sum_e [M_e]_{\text{lumped}}\frac{v_i^{\tau+\Delta\tau} - v_i^\tau}{\Delta\tau} = RHS_i - \sum_e [M_e]_{\text{cons}}\frac{3v_i^{\tau+\Delta\tau} - 4v_i^n + v_i^{n-1}}{2\Delta t}, \quad (28)$$

where $[M_e]_{\text{cons}} = \rho_o\int_{\mathcal{V}_e}[N]^T[N]\,d\mathcal{V}_o$ is the element consistent mass matrix and $[M_e]_{\text{lumped}}$ is the lumped mass matrix obtained from the HRZ lumping approach [56].

For the solid domain, a second-order accurate single-step procedure [57] is employed:

$$u_i^{\tau+\Delta\tau} = u_i^{\tau} + \Delta\tau\left(v_i^{\tau+\Delta\tau} - \frac{3u_i^{\tau+\Delta\tau} - 4u_i^{n} + u_i^{n-1}}{2\Delta t}\right) + \frac{1}{2}\Delta\tau^2 \frac{1}{\rho_o \mathcal{V}_m}\left(RHS_i|_{\overline{u}_i^{\tau}} - \sum_e [M_e]_{\text{cons}} \frac{3v_i^{\tau+\Delta\tau} - 4v_i^{n} + v_i^{n-1}}{2\Delta t}\mathcal{V}_m\right). \quad (29)$$

$$v_i^{\tau+\Delta\tau} = v_i^{\tau} + \frac{\Delta\tau}{\sum_e [M_e]_{\text{lumped}} \mathcal{V}_m}\left(RHS_i|_{\overline{u}_i^{\tau}} - \sum_e [M_e]_{\text{cons}} \frac{3v_i^{\tau+\Delta\tau} - 4v_i^{n} + v_i^{n-1}}{2\Delta t}\mathcal{V}_m\right). \quad (30)$$

where $\overline{u}^{\tau}$ denotes a projected displacement which is calculated as

$$\overline{u}_i^{\tau} = u_i^{\tau} + \Delta\tau\left(v_i^{\tau} - \frac{3u_i^{\tau+\Delta\tau} - 4u_i^{n} + u_i^{n-1}}{2\Delta t}\right). \quad (31)$$

3.3.3. Pseudo-timestep calculations

The pseudo-timestep local to each computational cell is to be determined in the interest of optimal convergence while ensuring a stable solution process. An accurate estimation is therefore required for which the following expression is employed:

$$\Delta\tau = \text{CFL}\left[\frac{|u_i - u_i^*| + c_{\text{unified}}}{\Delta x_i} + \kappa\frac{2\mu}{\rho\Delta x_i^2}\right]^{-1} \quad (32)$$

where CFL denotes the Courant-Friedrichs-Lewy number, Δx_i is the effective mesh spacing in direction i and κ is equal to 1 in the fluid domain and 0 in the solid domain. Further,

$$c_{\text{unified}} = \kappa c_{\tau} + (1-\kappa)\left(\sqrt{K/\rho_0} + \sqrt{\eta/\rho_0}\right). \quad (33)$$

Finally, in the case of transient analyses, we treat the dual-timestepping term implicitly, i.e., change τ to $\tau + \Delta\tau$ in (24) and (27), in order to maintain stability in cases where $\Delta\tau$ is comparable to or larger than Δt [58].

3.4. Fluid-solid interface treatment

At the fluid-solid interface, the following equations for traction, displacement and velocity are prescribed:

$$\begin{aligned} \tau_j &= pn_j - \sigma_{ij}n_i \\ u_j &= u_j^* = v_j \\ x_j^f &= x_j^s \end{aligned} \quad (34)$$

where the superscripts f and s respectively denote fluid and solid and n_i is the related normal unit vector pointing outward from the fluid domain. The above are prescribed as part of the pseudo-stepping iterative procedure in a manner which effects a stable solution process.

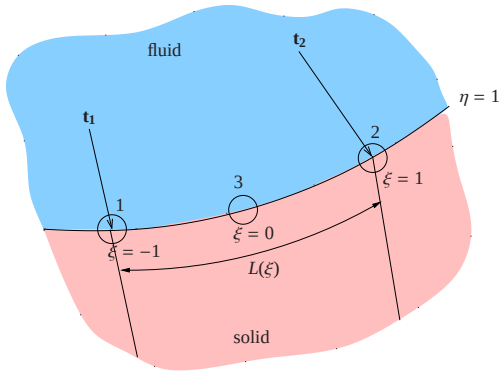

Figure 3: Arbitrary solid edge along the FSI interface.

3.4.1. Consistent nodal loads

For the purpose of this work fluid and solid interface nodes coincide, which simplifies the transfer of information between the fluid and solid domains. However, the Q8 element contains an additional node at the mid-point of every edge, which means there is an unconnected solid node for every element along the interface. Therefore, the transfer of traction from the fluid to the solid domain has to be evaluated in terms of conservation of momentum and accuracy on the overall solution [59, 60]. Two options exist: the traction from every fluid node on the interface is transferred to the corresponding solid node and the mid-nodes are ignored, which satisfies a global conservation of forces, or the traction from the fluid nodes are redistributed to every solid node, which locally is consistent with the finite element method. For the latter approach, and referring to Figure 3 which shows the traction imposed on an arbitrary solid edge along the FSI interface, the consistent FEM nodal loads are given by:

$$\{F\} = b \int_0^L [N]^T \mathbf{t} dL \tag{35}$$

where $[N]$ contains the shape functions associated with each node along the edge, L is the length of the edge and b is the depth of the element.

Assuming the traction $\mathbf{t}$ varies linearly between $\mathbf{t}_1$ and $\mathbf{t}_2$ (which is the case with the fluid discretisation [61]), Eq. (35) can be expanded as

$$\begin{Bmatrix} F_{1_{x_1}} \\ F_{1_{x_2}} \\ F_{2_{x_1}} \\ F_{2_{x_2}} \\ F_{3_{x_1}} \\ F_{3_{x_2}} \end{Bmatrix} = b \int_{-1}^{1} \begin{bmatrix} N_1 & 0 \\ 0 & N_1 \\ N_2 & 0 \\ 0 & N_2 \\ N_3 & 0 \\ 0 & N_3 \end{bmatrix} \left[S_1 \begin{Bmatrix} t_{1_{x_1}} \\ t_{1_{x_2}} \end{Bmatrix} + S_2 \begin{Bmatrix} t_{2_{x_1}} \\ t_{2_{x_2}} \end{Bmatrix} \right] \frac{dL}{d\xi} d\xi, \tag{36}$$

where the integral is transformed to the natural coordinate system and S_i are the linear shape functions assumed for the traction.

Substituting the quadratic shape functions associated with each node along the edge and simplifying gives

$$\begin{Bmatrix} F_{1_{x_1}} \\ F_{1_{x_2}} \\ F_{2_{x_1}} \\ F_{2_{x_2}} \\ F_{3_{x_1}} \\ F_{3_{x_2}} \end{Bmatrix} = b \int_{-1}^{1} \begin{bmatrix} -\frac{1}{2}\xi(1-\xi) & 0 \\ 0 & -\frac{1}{2}\xi(1-\xi) \\ \frac{1}{2}\xi(1+\xi) & 0 \\ 0 & \frac{1}{2}\xi(1+\xi) \\ (1-\xi^2) & 0 \\ 0 & (1-\xi^2) \end{bmatrix} \begin{Bmatrix} \frac{1}{2}(1-\xi)t_{1_{x_1}} + \frac{1}{2}(1+\xi)t_{2_{x_1}} \\ \frac{1}{2}(1-\xi)t_{1_{x_2}} + \frac{1}{2}(1+\xi)t_{2_{x_2}} \end{Bmatrix} \left(-\frac{1}{2}(1-2\xi)x_1 + \frac{1}{2}(1+2\xi)x_2 - 2\xi x_3 \right) d\xi. \quad (37)$$

The integrand is a fourth-order polynomial. Analytical integration gives the closed form expressions:

$$\begin{Bmatrix} F_{1_{x_1}} \\ F_{1_{x_2}} \\ F_{2_{x_1}} \\ F_{2_{x_2}} \\ F_{3_{x_1}} \\ F_{3_{x_2}} \end{Bmatrix} = \begin{Bmatrix} -\frac{b}{30}(13x_1t_{1_{x_1}} + 2x_1t_{2_{x_1}} + 3x_2t_{1_{x_1}} + 2x_2t_{2_{x_1}} - 16x_3t_{1_{x_1}} - 4x_3t_{2_{x_1}}) \\ -\frac{b}{30}(13x_1t_{1_{x_2}} + 2x_1t_{2_{x_2}} + 3x_2t_{1_{x_2}} + 2x_2t_{2_{x_2}} - 16x_3t_{1_{x_2}} - 4x_3t_{2_{x_2}}) \\ \frac{b}{30}(2x_1t_{1_{x_1}} + 3x_1t_{2_{x_1}} + 2x_2t_{1_{x_1}} + 13x_2t_{2_{x_1}} - 4x_3t_{1_{x_1}} - 16x_3t_{2_{x_1}}) \\ \frac{b}{30}(2x_1t_{1_{x_2}} + 3x_1t_{2_{x_2}} + 2x_2t_{1_{x_2}} + 13x_2t_{2_{x_2}} - 4x_3t_{1_{x_2}} - 16x_3t_{2_{x_2}}) \\ -\frac{b}{15}(7x_1t_{1_{x_1}} + 3x_1t_{2_{x_1}} - 3x_2t_{1_{x_1}} - 7x_2t_{2_{x_1}} - 4x_3t_{1_{x_1}} + 4x_3t_{2_{x_1}}) \\ -\frac{b}{15}(7x_1t_{1_{x_2}} + 3x_1t_{2_{x_2}} - 3x_2t_{1_{x_2}} - 7x_2t_{2_{x_2}} - 4x_3t_{1_{x_2}} + 4x_3t_{2_{x_2}}) \end{Bmatrix}. \quad (38)$$

The expressions above give the consistent FEM nodal loads for each node along the FSI interface as a function of the tractions imposed by the fluid domain.

3.5. Solution procedure

For the purpose of simultaneous solution of the discretised fluid-solid equations in a manner which effects strong coupling, the following solution sequence is employed in an iterative fashion:

1. The fluid and solid discrete equations are solved concurrently via a single iteration of (25), (29) and (30).
2. The calculated fluid traction is then applied to the solid boundary and the solid velocities to the fluid boundary.
3. The above is repeated until convergence, with the mesh only moved if a solid mesh boundary node displacement exceeds 30% of the element size or the residual of the fluid or solid mesh has been reduced by four orders of magnitude (a real-time-step is considered converged when the residual of all fluid and solid equations have dropped by at least 5 orders of magnitude).
4. The residuals are now calculated for all equations, and if larger than the convergence tolerance steps 1–3 are repeated.
5. If the residuals are below the convergence tolerance, the real-timestep is terminated, and the next time-step entered by proceeding to step 1.

4. Dynamic mesh movement

The mesh movement strategy employed is an interpolation procedure which, while offering no guarantees about element quality, has no significant computational cost and is well suited to parallel computing. This approach entails redistributing internal fluid nodes via the following interpolation function:

$$\Delta x_j = r\Delta x_j^1 + (1 - r)\Delta x_j^2,$$

where Δx_j^1 and Δx_j^2 denote the displacements of, respectively, the closest fluid node at the fluid-solid interface, and the closest external boundary node, from their initial locations. Also, r, which varies between zero and one, is computed as

$$r = \frac{D_2^p}{D_1^p + D_2^p} \quad \text{with } p = 3/2.$$

Here, D_1 and D_2 are the distances between the node being moved and its closest internal and external boundary points, respectively, in the undeformed configuration. This formula was tuned to the geometry of the large-displacement problems considered below, although it has been found to perform well for more general problems which involve small to moderate displacements. Since the closest points and the values of r are calculated only once at the beginning of the analysis, the application of the mesh movement function is essentially instantaneous, and the mesh will also not deteriorate due to repeated oscillations as it will always return to the initial configuration.

5. Parallelisation

Because of the fully matrix-free nature of the numerical method at solver subiteration level, data reference is local (nodes only see neighbouring nodes) meaning that the mesh can be decomposed into separate subdomains for parallel operation. As the operation count for each edge is very nearly identical, the number of edges in each domain was balanced for efficient operation. This is done by weighting each node with an integer equal to the number of edges which connect to it, followed by applying the METIS library [62] to its connectivity graph. For the purpose of interdomain communication, a system of "ghost nodes" is used in this work, with one layer of overlapping nodes at domain boundaries, where 'slave' nodes are updated with the values from corresponding 'master' nodes in the neighbouring domain. For efficiency, data transfer is consolidated into the largest possible packets and communicated using MPI.

An example of the overlap of domains due to the inclusion of ghost nodes is shown in Figure 4. The inset shows extended overlap near the boundary due to the larger stencil required for certain types of boundary conditions.

6. Application and evaluation

The developed FSI algorithms have been benchmarked with application to two-dimensional problems from the literature for which the results can be compared with

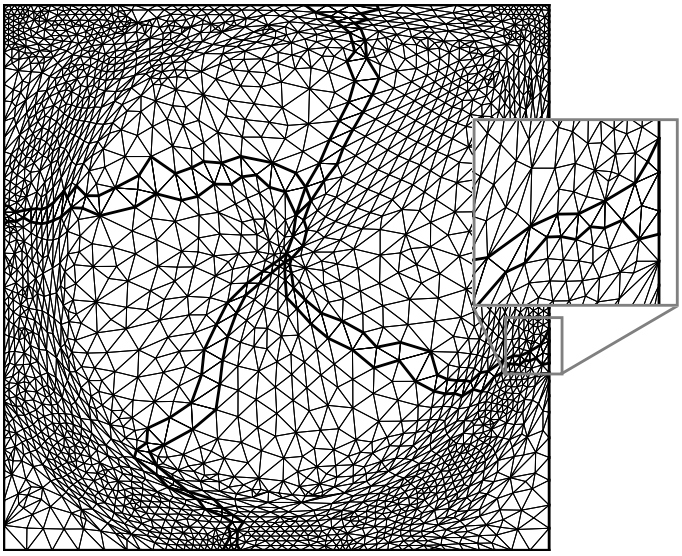

Figure 4: Example of domain decomposition showing one-element overlap due to ghost nodes and extended overlap near the boundaries.

analytical solutions or the results of others. The extension to three-dimensional problems follows easily, apart from the expected additional computational cost. The meshes employed range from structured to hybrid-unstructured, and solutions were only considered converged once the residual had been reduced by 5 orders of magnitude. Validation of the fluid solver for stationary meshes has previously been performed in [41].

6.1. Dynamic piston-channel system

The first test-case considered was that of a piston-channel system with a varying fluid domain. The system geometry and boundary conditions are described in Figure 5. The channel is 11 m long and is partially filled with an inviscid incompressible fluid with an elastic piston situated to its left. A prescribed velocity, $v(t)$, was imposed on the piston, which pushes the fluid out of the domain. A zero pressure boundary condition was imposed at the outflow boundary and slip boundary conditions were imposed along all the channel walls. The piston has a Young's modulus of $E = 10$ Pa and density and Poisson's ratio of zero. A linear elastic solid model was used for this problem for comparison with others [16]. The fluid has a density $\rho_f = 1$ kg m^{-3}.

This problem was chosen as the coupling between the fluid and solid domain is strong and partitioned FSI solution schemes usually diverge for such a problem, even with large under-relaxation [16, 47]. An analytical solution exists for this system, which can be considered as a simple 1D problem.

To obtain an analytical expression for the displacement and velocity of the interface, the system can be treated as a 1D spring-mass system, as shown in Figure 6. The

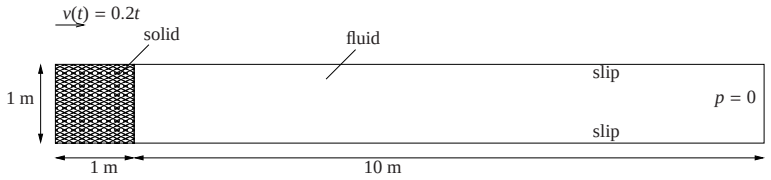

Figure 5: Geometry and boundary conditions for the piston-channel system.

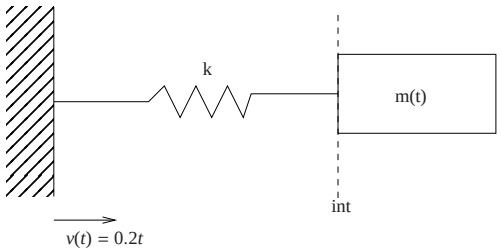

Figure 6: Representative spring-mass system for the piston-channel configuration.

elastic piston acts as a linear spring and the incompressible fluid as a variable mass [16]. Applying a balance of forces at the interface gives:

$$F_{\text{spring}} + F_{\text{mass}} = 0 \tag{39}$$

therefore,

$$k(u_{\text{int}} - u(t)) = -m\frac{dv_{\text{int}}}{dt} \tag{40}$$

where F_{spring} and F_{mass} are the forces exerted by the spring and mass, u_{int} and v_{int} are the displacement and velocity of the interface, $u(t)$ is the prescribed displacement of the left wall, k is the equivalent spring constant and m is the mass of the fluid. Substituting the properties of the piston and fluid for the spring and mass respectively, yield the following expressions for the velocity and displacement at the interface of the system:

$$\frac{dv_{\text{int}}}{dt} = \frac{10(u_{\text{int}} - 0.1t^2)}{(u_{\text{int}} - 10)} \tag{41}$$

$$\frac{du_{\text{int}}}{dt} = v_{\text{int}}. \tag{42}$$

The fluid domain is discretised using three cells. The solid domain is discretised using either a single finite volume cell or a single Q8 finite element. The resulting computed time history of the displacement and velocity of the interface is shown in Figure 7 for the finite volume method and in Figure 8 for the finite element method. As shown, both the schemes results in an accurate solution. In order to achieve stability for this problem, under-relaxation was necessary by reducing the CFL number by an

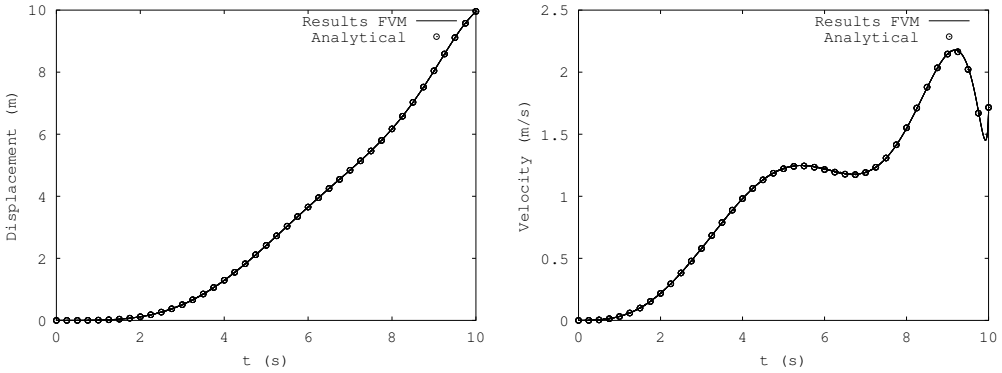

Figure 7: Displacement (left) and velocity (right) of the interface of the piston and channel using the finite volume method. The lines show the simulated response and the circles the analytical solution. This is identical to the result presented in [16].

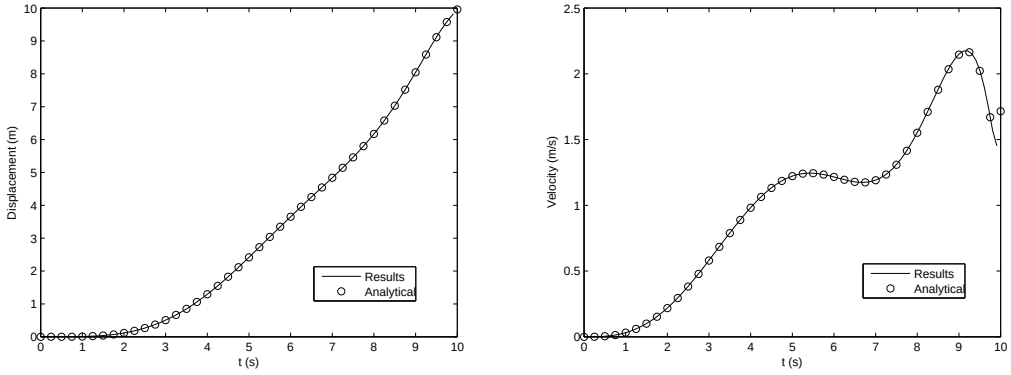

Figure 8: Displacement (left) and velocity (right) of the interface of the piston and channel using the finite element method.

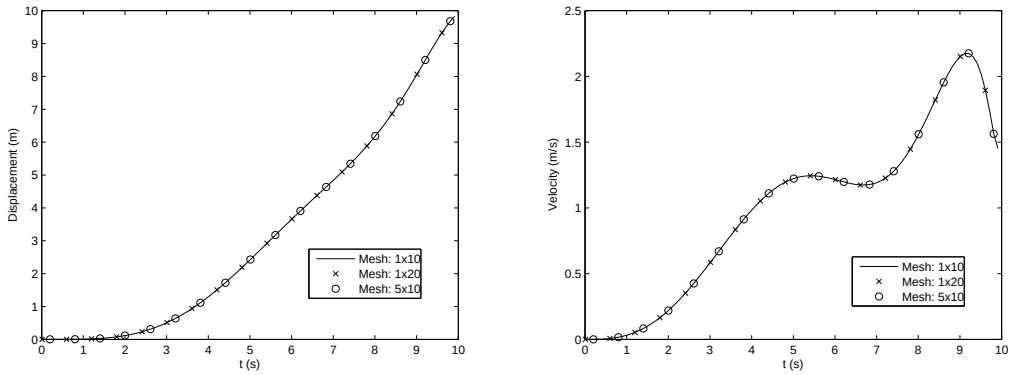

Figure 9: Displacement (left) and velocity (right) of the interface of the piston-channel using various meshes.

order of magnitude. However in all other more realistic FSI problems considered, no under-relaxation was found to be required.

Figure 9 shows the results obtained using different meshes for the fluid and solid domain, i.e. one solid and ten fluid cells (1×10), one solid and twenty fluid cells (1×20), and five solid and ten fluid cells (5×10). This demonstrates stability and robustness in the scheme.

Velocity contours of the solid and pressure contours of the fluid at various times are shown in Figure 10. The velocity field is linear in the solid, while the pressure field is linear in the fluid. A second-order accurate scheme is thus able to predict the solution exactly.

An investigation was conducted on this problem to determine the sensitivity of the average number of iterations required per time step with respect to the fluid-structure density ratio. The result, shown in Figure 11, indicates that the FSI system is less stable numerically when the density of the solid decreases, relative to the fluid. As the solid mass increases (or fluid density decreases) the so-called 'added mass effect' [63] becomes less significant and the system converges quicker.

6.2. Block-tail in first mode of vibration

The second test-case considered was that of an elastic beam in the wake of a rigid square block. This is a popular FSI benchmark test-case that was first proposed by Wall [64] and studied by many other researchers [16, 34, 18, 29]. In these publications, various different combinations of material properties, initial conditions and Reynolds numbers have been considered. In this work, we have considered the cases studied by Hübner *et al.* [16]. The geometry and boundary conditions are shown in Figure 12. The properties of the incompressible fluid are: density $\rho_f = 1.18 \times 10^{-3}$ g cm^{-3} and viscosity $\mu_f = 1.82 \times 10^{-4}$ g cm^{-1} s^{-1}, while that of the beam are: density $\rho_s = 2.0$ g cm^{-3}, Young's modulus $E = 2.0 \times 10^6$ g cm^{-1} s^{-2} and Poisson's ratio $\nu = 0.35$.

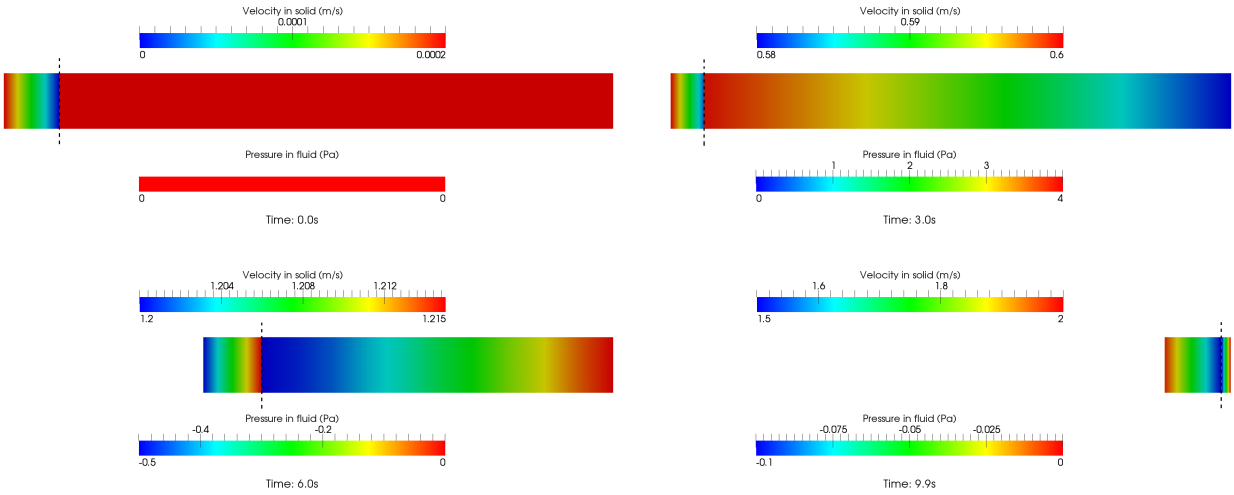

Figure 10: Velocity contours of the piston and pressure contours of the fluid at various times.

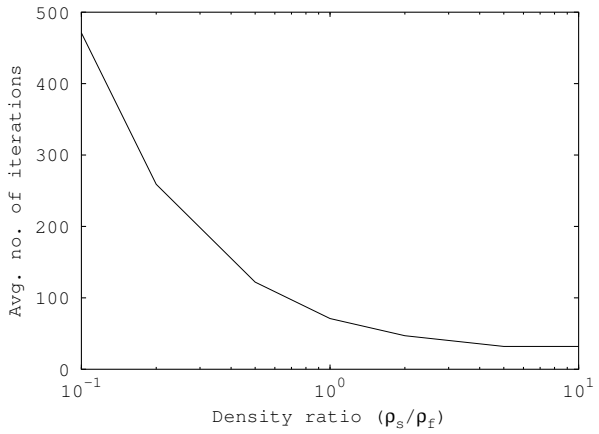

Figure 11: Sensitivity of average number of iterations per time-step with respect to fluid-structure density ratio.

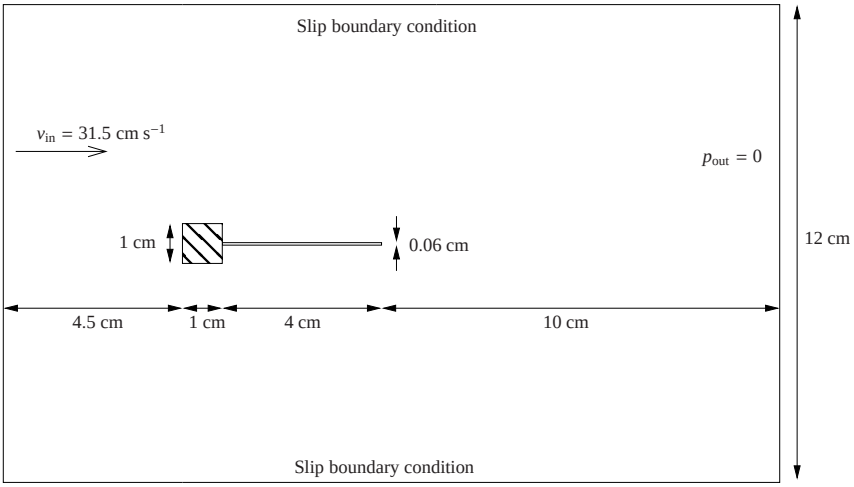

Figure 12: Geometry and boundary conditions for the block-tail FSI test-case.

Three meshes with varying density were employed (Figure 13) in the interests of finding a mesh-independent solution. The fluid meshes consist of 6 000, 25 000 and 50 000 fluid cells respectively. For the analyses using the finite volume method for the solid, structured meshes consisting of 12 elements through the thickness were employed, as this was found to produce a solution within 1% of the analytical solution for a static cantilever beam undergoing large displacements. The number of elements along the length of the beam was respectively selected as 40, 120 and 160 for the three different fluid meshes, in order to line up with the fluid nodes. In addition, to evaluate solution independence with respect to the solid mesh, an extra analysis was performed with a 320×24 solid mesh – i.e. half the mesh spacing in both directions – in conjunction with the 50 000 fluid mesh. With the finite element method for the solid, the structure was discretised using a single layer of 40 Q8 elements and a finer mesh of 80×2 Q8 elements was used to evaluate mesh independence. The time-step size used in the aforementioned analyses was $\Delta t = 0.001$ s, and the accuracy of this was verified by comparing with additional analyses with varying time-step sizes.

The beam was given an initial deflection due to a temporary load and the plane strain assumption was used. This problem was considered by Hubner et al. [16]. In order to fit the initial deflection of the beam as shown in [16], the piecewise-constant tip-load as a function of time was determined empirically and is shown in Table 1.

The large deflection of the beam causes a vortex to develop on the opposite side of the deflection. This vortex moves along the beam and breaks away as the beam reaches its maximum deflection. As the beam moves in the other direction, a smaller vortex of opposite rotation develops at its tip and also breaks away. Large-amplitude oscillations of the beam occur in its first mode of vibration. Plots of the pressure and velocity contours are shown in Figure 14.

The tip displacement of the beam is compared with the results of Hubner et al. [16]

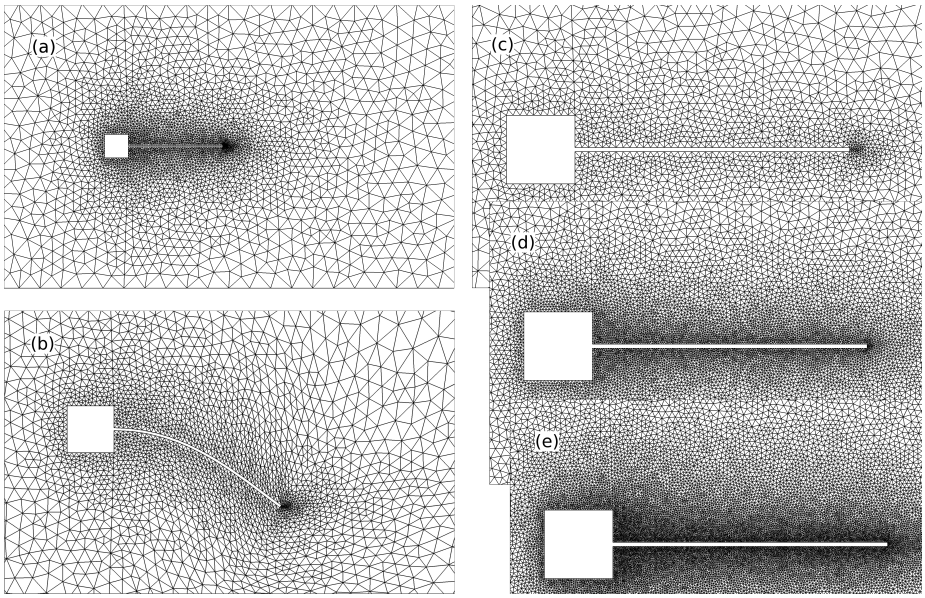

Figure 13: Block with flexible tail: (a) 6 000 cell mesh; (b) example of deformed mesh; (c-e) Close up views of 6 000, 25 000 and 50 000 cell meshes respectively.

Time (s):	0–0.1	0.1–0.15	0.15–0.2	0.2–0.3	0.3–0.4	0.4–0.5	0.5–0.6
Force (g cm s^{-2}):	0	0.35	1.5	2.3	3.1	4.2	6.5
Time (s):	0.6–0.7	0.7–0.8	0.8–0.9	0.9–1.0	1.0–1.1	1.1–1.2	1.2–1.3
Force (g cm s^{-2}):	6.5	5.5	5.0	4.0	3.0	2.0	1.0

Table 1: Piecewise-constant force as a function of time applied to tip of beam to reproduce initial deflection in results of [16].

in Figure 15 using the finite volume method and in Figure 16 using the finite element method. The finite volume and finite element FSI formulations provide very similar results. When compared with published data [16], there is a difference in the initial response, but the results compare well as the limit-cycle is reached. Since the details of the initial conditions imposed on the flow and the solid in [16] are not known, the initial discrepancy is not considered significant. A rigorous mesh and temporal independence study was conducted. To evaluate mesh independence of the fluid, the simulations were carried out on all three fluid meshes and the results shown in Figure 15(b) and Figure 16(b). There is a significant change in the solution from the 6 000 to the 25 000 element mesh, but negligible change between the 25 000 and 50 000 element mesh. Next, temporal independence was evaluated by using four different timestep sizes varying from 0.005s to 0.0005s. The time history in Figure 15(c) and Figure 16(c) show good convergence and independence in the results. Finally, to evaluate mesh independence of the solid a finer solid mesh twice the size was used and it was found that the results are identical to the coarser solid mesh case (see Figure 15(d)

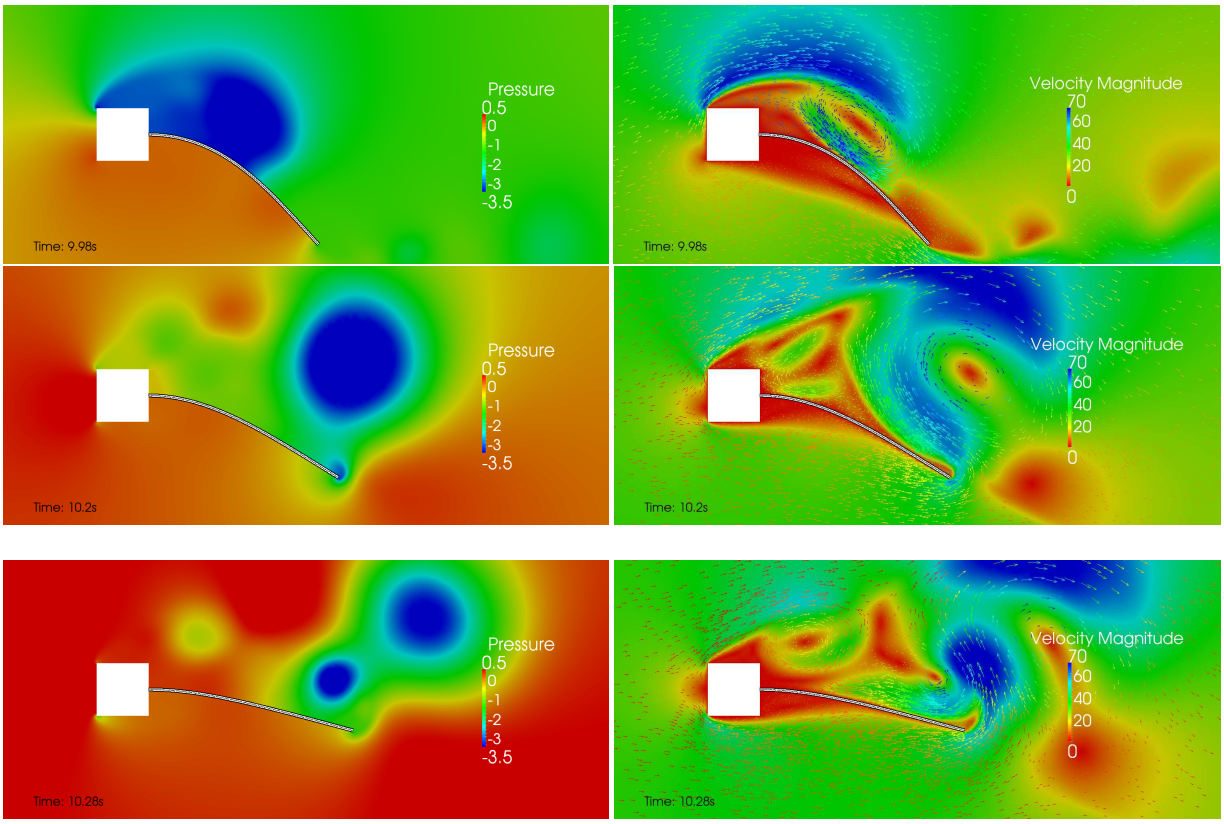

Figure 14: Pressure (left) and velocity contours (right) for the block-tail test-case with the beam oscillating in its first mode of vibration.

and Figure 16(d)). A comparison of the frequency and amplitude for different meshes and timestep sizes is shown in Table 2 for the finite volume method and in Table 3 for the finite element method.

6.3. Block-tail in second mode of vibration

In the final test-case, the same block-tail geometry as above was considered but a uniform constant fluid velocity, $v_{\text{in}} = 31.5$ cm s^{-1}, or Reynolds number, $Re = \frac{\rho_f L v_{in}}{\mu_f} = 204$, was applied at the inlet while at the exit the pressure was set to zero. The plane stress assumption was used. The inlet velocity results in vortices that are shed from the corners of the block periodically at a frequency of 3.7 Hz, which is close to the second natural frequency of the beam of 3.8 Hz. The fluid passes over the beam as symmetric vortices develop on either side of it. The symmetry of the vortices breaks, which results in uneven forces on the beam inducing vibrations of small amplitude. The oscillation of the beam results in further disturbance of the flow, which in turn

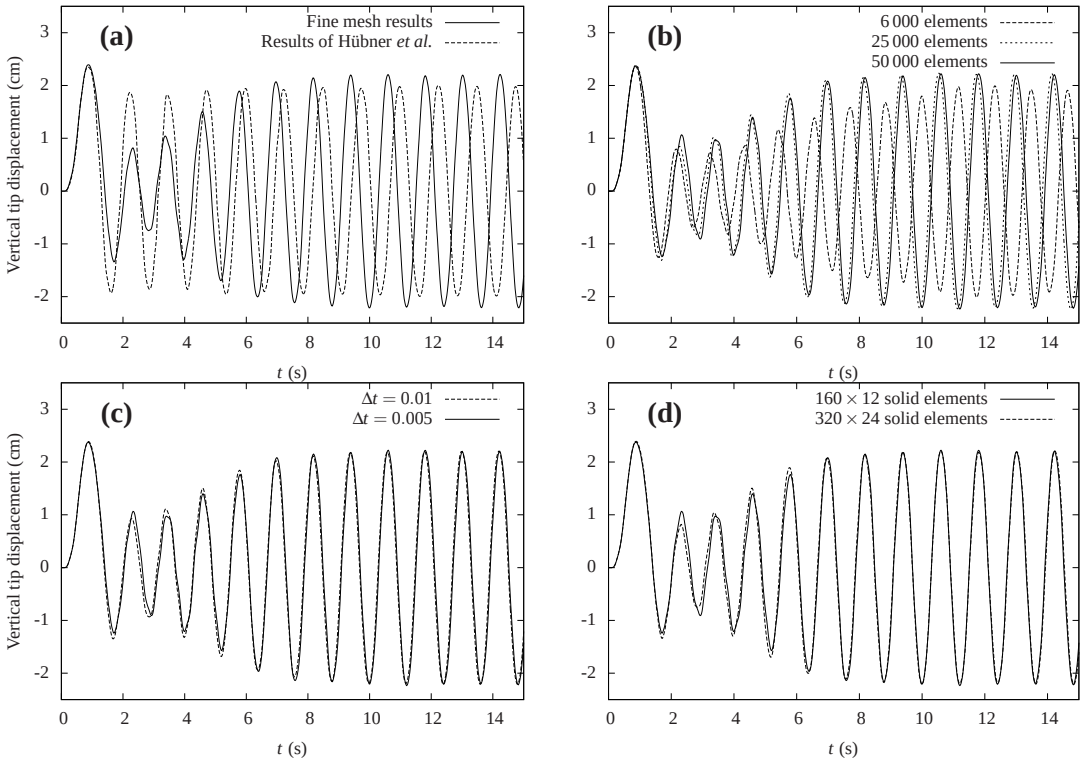

Figure 15: Tip deflection of block with flexible tail using the finite volume method with initial tip load given in Table 1. (a) Results on the 50 000 node fluid mesh and 320×24 solid mesh with a timestep size $\Delta t = 0.005$ s compared with the results of Hübner *et al.* [16]. (b) 6 000, 25 000 and 50 000 element fluid meshes with 40×12, 120×12 and 160×12 solid elements respectively. $\Delta t = 0.005$ s. (c) 160×12 and 320×24 element solid meshes. 50 000 fluid elements and $\Delta t = 0.005$ s. (d) $\Delta t = 0.01$ and $\Delta t = 0.005$ s with 50 000 fluid elements and 160×12 solid elements.

Fluid mesh	Solid mesh	Timestep (s)	Amplitude (cm)	Frequency (Hz)
6 000	40×12	0.005	2.03	0.86
25 000	120×12	0.005	2.22	0.83
50 000	160×12	0.01	2.22	0.83
50 000	160×12	0.005	2.21	0.83
50 000	320×24	0.005	2.20	0.82
Hubner et al. [16]			1.98	0.79

Table 2: Comparison of amplitude and frequency of limit-cycle oscillation for the block-tail test-case in first mode of vibration with various meshes and timestep sizes using the finite volume method.

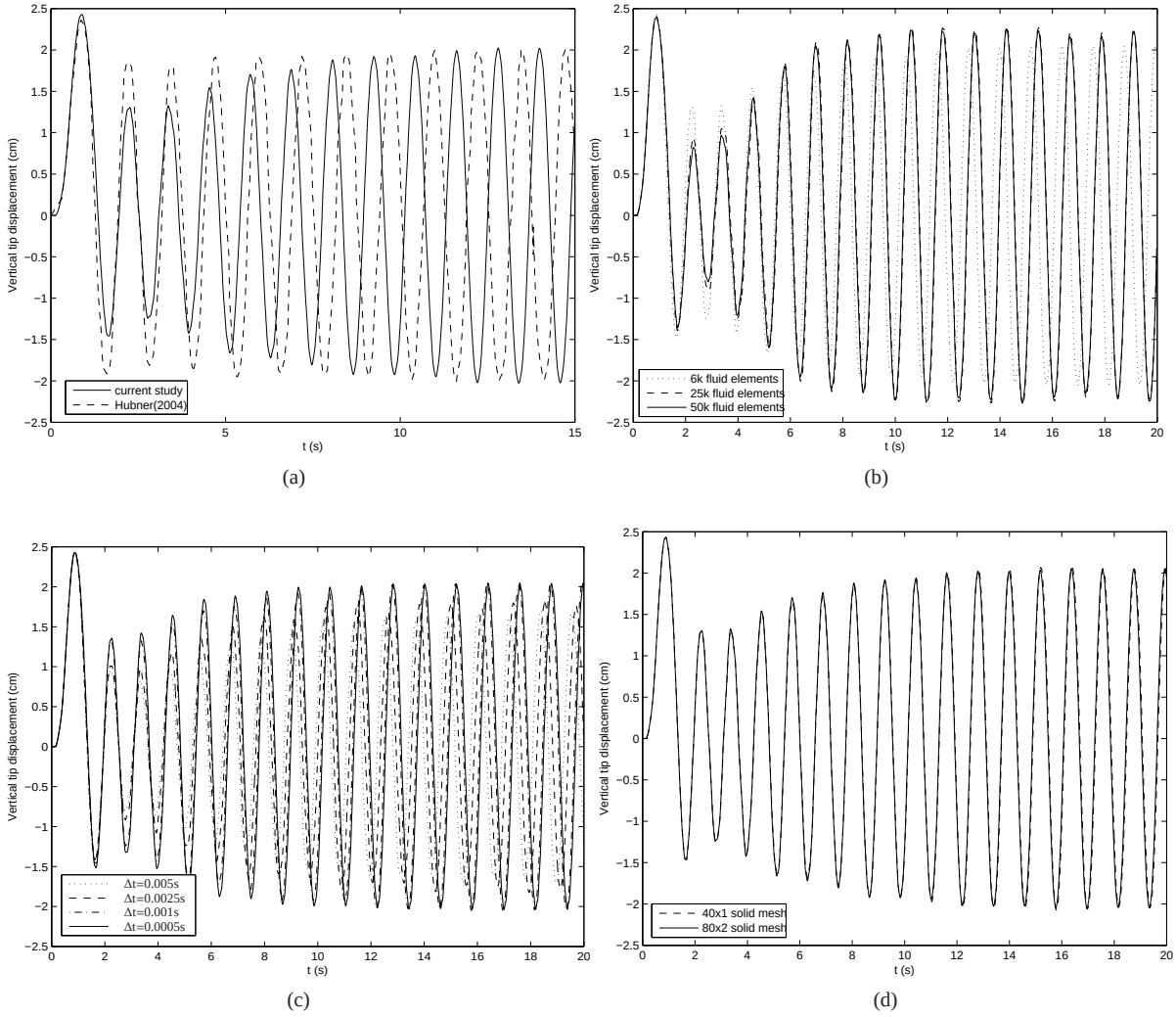

Figure 16: Tip displacement for the block-tail test-case in first mode of vibration with various meshes and timestep sizes using the finite element method.

Fluid mesh	Solid mesh	Timestep (s)	Amplitude (cm)	Frequency (Hz)
6 000	40×1	0.001	2.04	0.84
6 000	80×2	0.001	2.04	0.84
25 000	120×1	0.001	2.17	0.83
50 000	160×1	0.001	2.18	0.82
6 000	40×1	0.0005	2.04	0.84
Hubner et al. [16]			1.98	0.79

Table 3: Comparison of amplitude and frequency of limit-cycle oscillation for the block-tail test-case in first mode of vibration with various meshes and timestep sizes using the finite element method.

induces larger displacements of the beam. Within each period, two vortices develop on one side of the beam while a larger vortex develops on the other side, as shown in Figure 17. The system builds up to large oscillations of the beam in its second mode of vibration as vortices are shed periodically from either side of it.

The finite volume and finite element FSI formulations, once again, produced very similar results. Using the finite volume method FSI formulation, the 25 000-element fluid mesh and 160×12 solid mesh for this problem, and a time-step of $0.001s$, the expected match of results compared to those reported in [16] are shown in Figure 18: The amplitude (0.76 cm) and frequency ($2.87\,s^{-1}$) of second-mode vibrations are within 4% and 7% respectively. Note that the results of Hübner *et al.* were temporally offset to align limit state results. This is because the initial onset of the oscillations is thought to be an artifact of a particular numerical scheme as the system is in a state of unstable equilibrium to begin with. Using the finite element formulation, the time history of the tip displacement of the beam is plotted in Figure 19(a), together with the results of Hubner et al. [16]. There is a good correlation between the two sets of results, with the amplitude and frequency differing by less than 3% and 4% respectively as shown in Table 4. A comparison of the results using three fluid meshes of 6 000, 25 000 and 50 000 elements is shown in Figure 19(b). A small change in solution is observed from the 6 000 to the 25 000 element mesh, but a further doubling of the number of elements results in a negligible difference. Next, to evaluate mesh independence of the solid a finer solid mesh of 80×2 Q8 elements was used and it was found that the results are identical to the 40×1 solid mesh case (see Figure 19(c)). Finally, temporal independence was evaluated by using four different timestep sizes varying from 0.005s to 0.0005s. The time history in Figure 19(d) as well as the result in Table 4 show good convergence and independence in the results. The frequency and amplitude for different meshes and timestep sizes are summarised in Table 4.

6.4. Consistent nodal loads

An evaluation of the transfer of traction forces from the fluid to the solid domain was conducted. Since the Q8 element contains an additional node at the mid-point of every edge there is an additional unconnected solid node at the FSI interface. This complicates the transfer of the traction forces: either the traction at every fluid node on the interface is transferred to the corresponding solid node, which will satisfy a

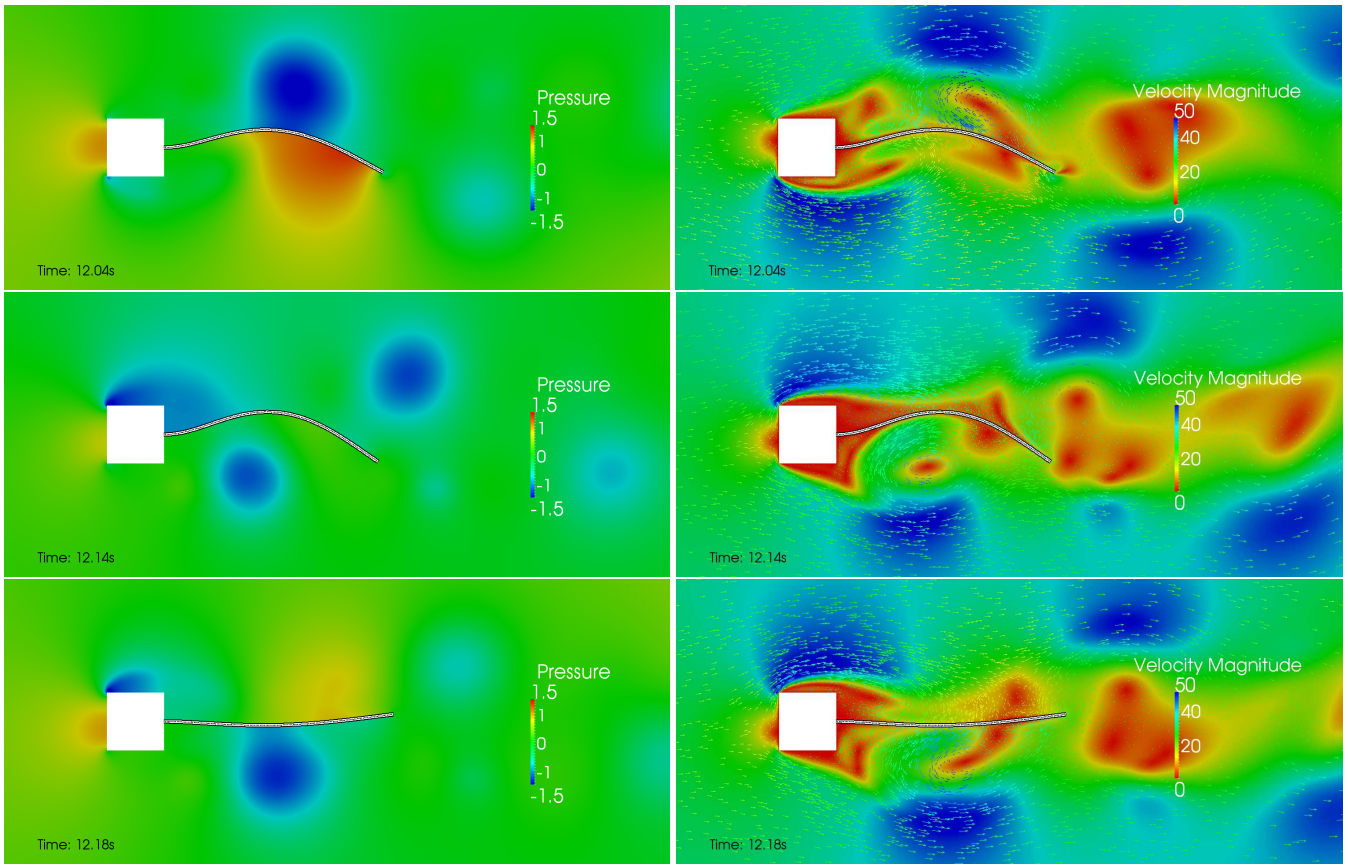

Figure 17: Pressure (left) and velocity contours (right) for the block-tail test-case with the beam oscillating in its second mode of vibration.

global balance of force, or FEM nodal loads, as described in the previous section and which are consistent with the finite element method, are calculated and the traction distributed to every solid node at the interface. Both approaches were implemented and a comparison of the tip displacement is shown in Figure 20. There is a negligible change in result and for practical purposes a simple transfer of traction from every fluid node to the corresponding solid node on the interface is sufficient, if structural stresses on the interface are not of primary concern.

6.5. Parallel efficiency

The evaluation of parallelisation speed-up is of particular importance to this work, as it serves to assess the value and impact of the purely matrix-free edge-based methodology developed. This was done by considering the reduction in wall-clock time in performing a set number of iterations. Problem sizes of 9 000 and 25 000 elements were

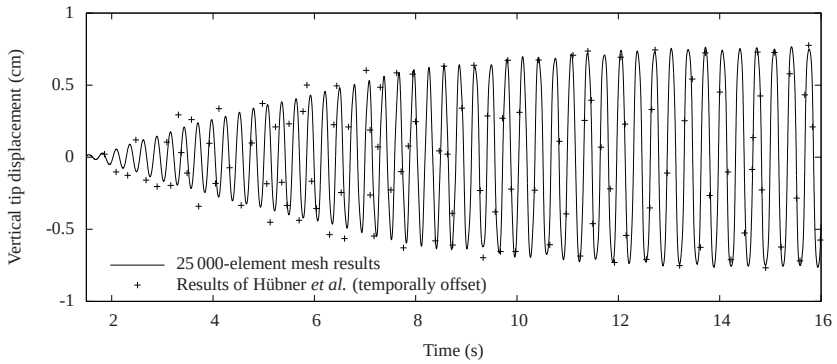

Figure 18: Tip deflection of block with flexible tail using the finite volume method with no initial tip load compared to the results of Hübner *et al.* [16].

Fluid mesh	Solid mesh	Timestep (s)	Amplitude (cm)	Frequency (Hz)
6 000	40×1	0.001	0.78	2.98
6 000	80×2	0.001	0.78	2.98
25 000	120×1	0.001	0.76	2.97
50 000	160×1	0.001	0.76	2.97
6 000	40×1	0.0005	0.78	2.97
Hubner et al. [16]			0.8	3.1
Xia et al. [29]			0.81	3.3

Table 4: Comparison of amplitude and frequency for the block-tail test-case in second mode of vibration using the finite element method with various meshes and timestep sizes.

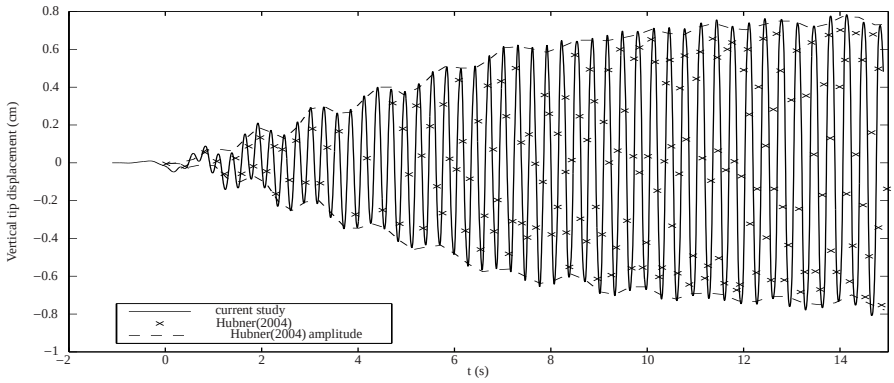

(a)

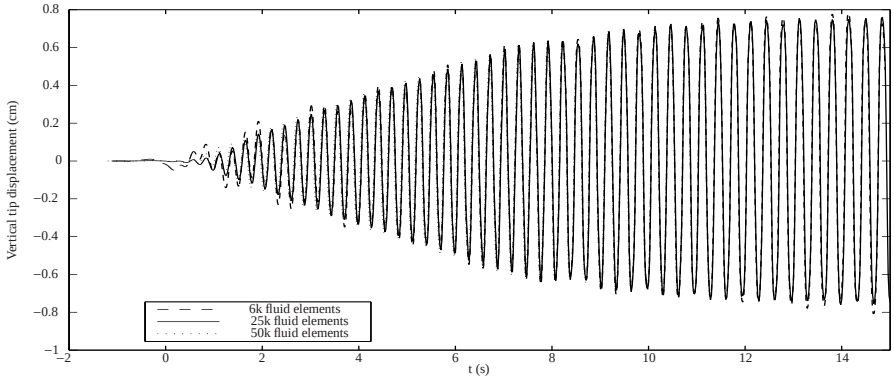

(b)

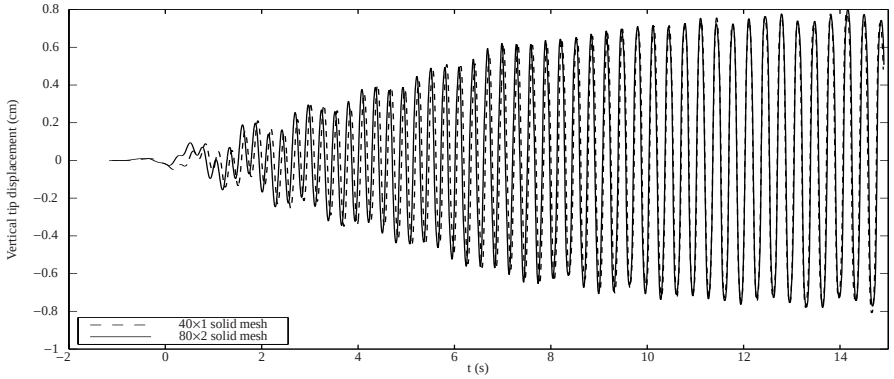

(c)

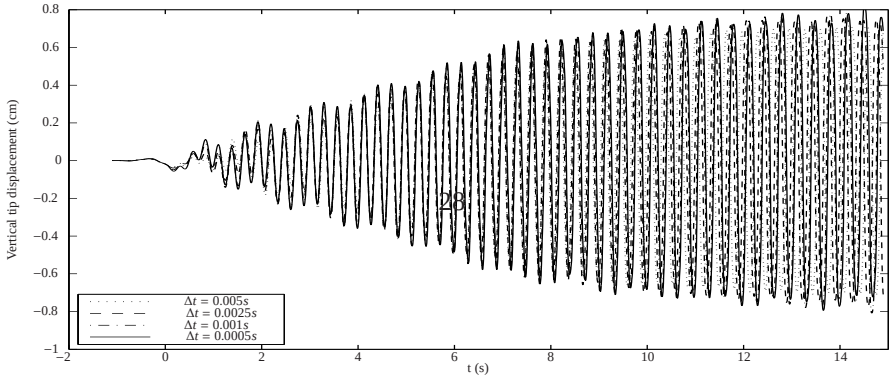

(d)

Figure 19: Tip displacement for the block-tail test-case in second mode of vibration using the finite element method with various meshes and timestep sizes.

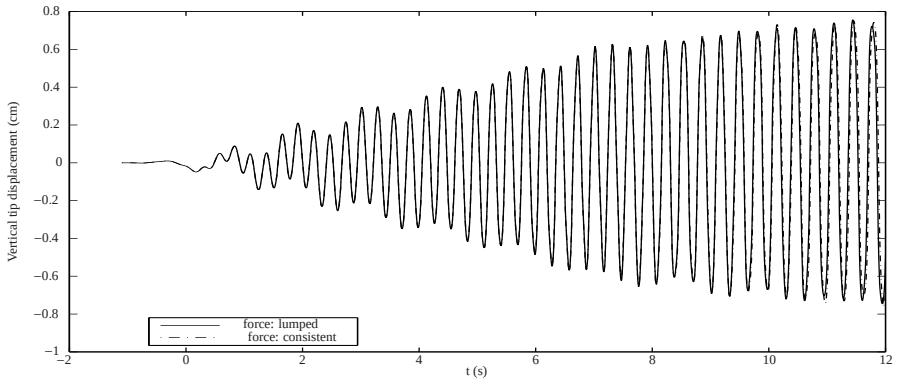

Figure 20: Tip displacement for the block-tail test-case in second mode of vibration using consistent and lumped traction forces at the interface.

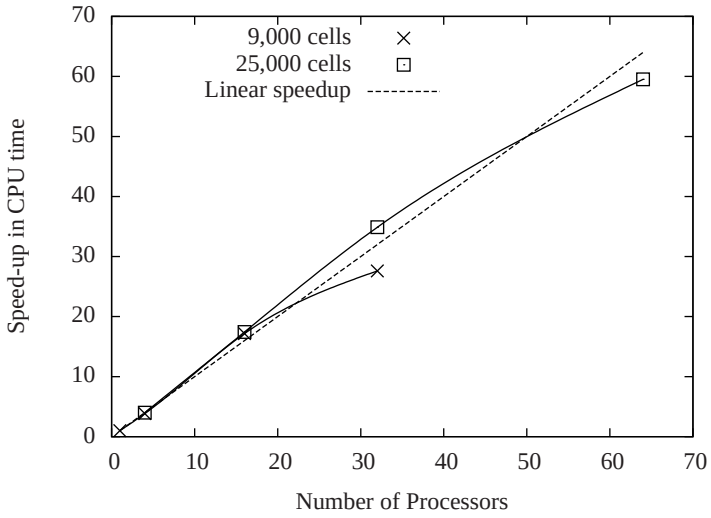

Figure 21: Parallelisation speed-up for the block-tail problem.

considered. Calculations were perfomed on an IBM E1350 cluster with AMD Opteron 2.6 GHz processors and Infiniband interconnects at the Centre for High Performance Computing (CHPC), Cape Town.

The results of the study are depicted in Figure 21, where the number of iterations achieved per second has been normalised to the value for a single processor. As shown, increasing the number of CPUs results in a super-linear speed-up region followed by the eventual loss in parallel performance due to inter-core communication becoming dominant over computing time, which occurs only if assigning less than circa 500

elements to a CPU.

7. Conclusions

In this paper we have developed a partitioned scheme to model the interaction of incompressible viscous fluids with homogeneous elastic solids undergoing large non-linear displacements. In the case of the fluid, an ALE Artificial Compressibility Characteristic Based Split (CBS-AC) algorithm was developed, and discretised via an edge-based hybrid-unstructured compact vertex-centered finite volume methodology. For the solid, both a hybrid elemental/nodal-strain approach and isoparametric Q8 finite element methodology were used and solved via a matrix-free dual-timestepping approach. The entire fluid/solid system is solved in a manner which prioritises scalable, matrix-free parallel computing. Coupling is on the solver sub-iteration level leading to a tighter coupling than if the subdomains are converged separately. The scheme was evaluated by application to benchmark problems for strongly-coupled fluid-structure interaction problems. It was demonstrated to effect full coupling between the fluid and solid domains, whilst furnishing accurate solutions in all cases.

References

[1] A. Slone, K. Pericleous, C. Bailey, M. Cross, C. Bennett, A finite volume unstructured mesh approach to dynamic fluid-structure interaction: an assessment of the challenge of predicting the onset of flutter, Applied Mathematical Modelling 28 (2004) 211–239.

[2] C. Farhat, M. Lesoinne, Two efficient staggered algorithms for the serial and parallel solution of three-dimensional nonlinear transient aeroelastic problems, Computer Methods in Applied Mechanics and Engineering 182 (2000) 499–515.

[3] R. van Loon, F. N. van de Vosse, Special issue: Fluidstructure interaction in biomedical applications, International Journal for Numerical Methods in Biomedical Engineering 26 (3-4) (2010) 273–275. doi:10.1002/cnm.1371.

[4] C. Taylor, C. Figueroa, Patient-specific modeling of cardiovascular mechanics, Annual Review of Biomedical Engineering 11 (1) (2009) 109–134. doi:10.1146/annurev.bioeng.10.061807.160521.

[5] J. Hron, M. Madlik, Fluid-structure interaction with applications in biomechanics, Nonlinear Analysis: Real World Applications 8 (2007) 1431–1458.

[6] E. Järvinen, P. Råback, M. Lyly, J.-P. Salenius, A method for partitioned fluid–structure interaction compution of flow in arteries, Medical Engineering & Physics 30 (2008) 917–923.

[7] K.-J. Paik, P. Carrica, D. Lee, K. Maki, Strongly coupled fluid-structure interaction method for structural loads on surface ships, Ocean Engineering 36 (2009) 1346–1357.

[8] B. Sreejith, K. Jayaraj, N. Ganesan, C. Padmanabhan, P. Chellapandi, P. Selvaraj, Finite element analysis of fluid-structure interaction in pipeline systems, Nuclear Engineering and Design 227 (3) (2004) 313 – 322.

[9] A. L. Braun, A. M. Awruch, Aerodynamic and aeroelastic analyses on the CAARC standard tall building model using numerical simulation, Computers and Structures 87 (910) (2009) 564 – 581.

[10] W. A. Wall, E. Ramm, Fluid-structure interaction based upon a stabilized (ALE) finite element method, in: S. Idelsohn, E. Oñate, E. Dvorkin (Eds.), Computational mechanics – new trends and applications, Proceedings of WCCM IV, CIMNE, Barcelona, 1998.

[11] K. J. Bathe, H. Zhang, S. Ji, Finite element analysis of fluid flows fully coupled with structural interactions, Computers and Structures 72 (1-3) (1999) 1–16. doi:10.1016/S0045-7949(99)00042-5.

[12] E. H. Dowell, K. C. Hall, Modeling of fluid-structure interaction, Annual Review of Fluid Mechanics 33 (1) (2001) 445–490. doi:10.1146/annurev.fluid.33.1.445.

[13] R. Ohayon, C. F. (Eds.), Special issue: Advances in computational methods for fluidstructure interaction and coupled problems, Computer Methods in Applied Mechanics and Engineering 190 (2001) 2977–3292. doi:10.1016/S0045-7825(00)00376-5.

[14] T. Tezduyar, Y. Bazilevs, Special issue on fluid–structure interaction, Computational Mechanics 43 (2008) 1–189.

[15] A. G. Malan, Investigation into the continuum thermodynamic modeling of investment casting shell-mould drying, Ph.D. thesis, University of Wales Swansea (2002).

[16] B. Hubner, E. Walhorn, D. Dinkler, A monolithic approach to fluid-structure interaction using space-time finite elements, Computer Methods in Applied Mechanics and Engineering 193 (2004) 2087–2104.

[17] C. G. H. Weller, A unified formulation for continuum mechanics applied to fluid-structure interaction in flexible tubes, International Journal for Numerical Methods in Engineering 64 (2005) 1575–1593.

[18] W. Dettmer, J. Peric, A computational framework for fluid-structure interaction: Finite element formulation and application, Computer Methods in Applied Mechanics and Engineering 195 (2006) 5754–5779.

[19] W. A. Wall, S. Genkinger, E. Ramm, A strong coupling partitioned approach for fluid–structure interaction with free surfaces, Computers and Fluids 36 (2007) 169–183.

[20] J. Degroote, R. Haelterman, S. Annerel, P. Bruggeman, J. Vierendeels, Performance of partitioned procedures in fluid-structure interaction, Computers and Structures 88 (2010) 446–457.

[21] M. von Scheven, E. Ramm, Strong coupling schemes for interaction of thin-walled structures and incompressible flows, International Journal for Numerical Methods in Engineering 87 (2011) 214–231.

[22] U. Küttler, W. A. Wall, Fixed-point fluid–structure interaction solvers with dynamic relaxation, Computational Mechanics 43 (2008) 61–72.

[23] D. P. Mok, W. A. Wall, Partitioned analysis schemes for the transient interaction of incompressible flows and nonlinear flexible structures, in: W. A. Wall, K.-U. Bletzinger (Eds.), Trends in computational structural mechanics, Barcelona: CIMNE, 2011, pp. 689–698.

[24] P. L. Tallec, J. Mouro, Fluid structure interaction with large structural displacements, Computer Methods in Applied Mechanics and Engineering 190 (2001) 3039–3067.

[25] H. G. Matthies, J. Steindorf, Partitioned strong coupling algorithms for fluid–structure interaction, Computers and Structures 81 (2003) 805–812.

[26] J. Vierendeels, L. Lanoye, J. Degroote, P. Verdonck, Implicit coupling of partitioned fluid-structure interaction problems with reduced order models, Computers and Structures 85 (2007) 970–976.

[27] J. Degroote, K. J. Bathe, J. Vierendeels, Performance of a new partitioned procedure versus a monolithic procedure in fluid-structure interaction, Computers and Structures 87 (2009) 793–801.

[28] A. Slone, K. Pericleous, C. Bailey, M. Cross, Dynamic fluid-structure interaction using finite volume unstructured mesh procedures, Computers and Structures 80 (2002) 371–390.

[29] G. Xia, C.-L. Lin, An unstructured finite volume approach for structural dynamics in response to fluid motions, Computers and Structures 86 (2008) 684–701.

[30] X. Lv, Y. Zhao, X. Huang, G. Xia, X. Su, A matrix-free implicit unstructured multigrid finite volume method for simulating structural dynamics and fluid-structure interaction, Journal of Computational Physics 225 (2007) 120–144.

[31] Z. He, G. Liu, Z. Zhong, G. Zhang, A. Cheng, Coupled analysis of 3D structural-acoustic problems using the edge-based smoothed finite element method/finite element method, Finite Elements in Analysis and Design 46 (2010) 1114–1121.

[32] S. Mitra, K. Sinhamahapatra, 2D simulation of fluid-structure interaction using finite element method, Finite Elements in Analysis and Design 45 (2008) 52–59.

[33] T. Tezduyar, S. Sathe, R. Keedy, K. Stein, Space-time finite element techniques for computation of fluid-structure interactions, Computer Methods in Applied Mechanics and Engineering 195 (2006) 2002–2027.

[34] P. Texeira, A. Awruch, Numerical simulation of fluid-structure interaction using the finite element method, Computers and Fluids 34 (2005) 249–273.

[35] R. Suliman, O. Oxtoby, A. Malan, S. Kok, An enhanced matrix-free edge-based finite volume approach to model structures, in: S. Kok, D. Wilke, H. Inglis (Eds.), In proceedings: The 7^{th} South African Conference on Computational and Applied Mechanics (SACAM10), Pretoria, South Africa, 10-13 January 2010, pp. 399–406.

[36] R. Suliman, O. Oxtoby, A. Malan, S. Kok, An enhanced finite volume method to model 2D linear elastic structures, Applied Mathematical Modelling 38 (2014) 2265–2279.

[37] A. G. Malan, R. W. Lewis, Modeling coupled heat and mass transfer in drying non-hygroscopic capillary particulate materials, Communications in Numerical Methods in Engineering 19 (9) (2003) 669–677.

[38] P. I. Crumpton, P. Moinier, M. B. Giles, An unstructured algorithm for high Reynolds number flows on highly stretched meshes, in: C. Taylor, J. T. Cross (Eds.), Numerical Methods in Laminar and Turbulent Flow, Pineridge Press, 1997, pp. 561–572.

[39] Y. Zhao, B. Zhang, A high-order characteristics upwind FV method for incompressible flow and heat transfer simulation on unstructured grids, Computer Methods in Applied Mechanics and Engineering 190 (57) (2000) 733 – 756.

[40] A. G. Malan, R. W. Lewis, P. Nithiarasu, An improved unsteady, unstructured, artificial compressibility, finite volume scheme for viscous incompressible flows: Part I. Theory and implementation, International Journal for Numerical Methods in Engineering 54 (5) (2002) 695–714.

[41] A. G. Malan, R. W. Lewis, An artificial compressibility CBS method for modelling heat transfer and fluid flow in heterogeneous porous materials, International Journal for Numerical Methods in Engineering 87 (2011) 412–423.

[42] P. Nithiarasu, An efficient artificial compressibility (ac) scheme based on the characteristic based split (cbs) method for incompressible flow, International Journal for Numerical Methods in Engineering 56 (13) (2003) 1815–1845.

[43] P. Nithiarasu, An arbitrary Lagrangian Eulerian (ALE) formulation for free surface flows using the characteristic-based split (CBS) scheme, International Journal for Numerical Methods in Fluids 48 (2005) 1415–1428.

[44] S. V. Patankar, Numerical Heat Transfer and Fluid Flow, McGraw-Hill, New York, 1980.

[45] A. J. Chorin, A numerical method for solving incompressible viscous flow problems, Journal of Computational Physics 2 (1967) 12–26.

[46] C. Hirt, A. Amsden, J. Cook, An arbitrary Lagrangian-Eulerian computing method for all flow speeds, Journal of Computational Physics 14 (1974) 227–253.

[47] K. Bathe, G. Ledezma, Benchmark problems for incompressible fluid flows with structural interactions, Computers and Structures 85 (2007) 628–644.

[48] T. Tezduyar, M. Behr, J. Liou, A new strategy for finite element computations involving moving boundaries and interfaces–the deforming-spatial-domain/space-time procedure: I. the concept and the preliminary numerical tests, Computer Methods in Applied Mechanics and Engineering 94 (3) (1992) 339 – 351.

[49] T. Tezduyar, M. Behr, S. Mittal, J. Liou, A new strategy for finite element computations involving moving boundaries and interfaces–the deforming-spatial-domain/space-time procedure: Ii. computation of free-surface flows, two-liquid flows, and flows with drifting cylinders, Computer Methods in Applied Mechanics and Engineering 94 (3) (1992) 353 – 371.

[50] X. Wang, An iterative matrix-free method in implicit immersed boundary/continuum methods, Computers and Structures 85 (11–14) (2007) 739 – 748.

[51] R. van Loon, P. Anderson, F. van de Vosse, S. Sherwin, Comparison of various fluid-structure interaction methods for deformable bodies, Computers and Structures 85 (11–14) (2007) 833 – 843.

[52] G. Holzapfel, Nonlinear Solid Mechanics: A continuum Approach for Engineering., John Wiley & Sons Ltd., West Sussex, England, 2001.

[53] P. D. Thomas, C. K. Lombard, Geometric conservation law and its application to flow computations on moving grids, AIAA Journal (17) (1979) 1030–1037.

[54] M. Lesoinne, C. Farhat, Geometric conservation laws for flow problems with moving boundaries and deformable meshes, and their impact on aeroelastic computations, Computer Methods in Applied Mechanics and Engineering (134) (1996) 71–90.

[55] K. A. Sørensen, O. Hassan, K. Morgan, N. P. Weatherill, Agglomerated multigrid on hybrid unstructured meshes for compressible flow, International Journal for Numerical Methods in Fluids 40 (3-4) (2002) 593–603.

[56] R. D. Cook, D. S. Malkus, M. E. Plesha, R. J. Witt, Concepts and Applications of Finite Element Analysis, 4th Edition, John Wiley & Sons Ltd., United States, 2002.

[57] O. C. Zienkiewicz, R. L. Taylor, The Finite Element Method: Volume 2 - Solid Mechanics, 5th Edition, Butterworth-Heinemann, Oxford, 2000.

[58] V. Venkatakrishnan, D. J. Mavriplis, Implicit method for the computation of unsteady flows on unstructured grids, Journal of Computational Physics 127 (1996) 380–397.

[59] C. Farhat, M. Lesoinne, P. LeTallec, Load and motion transfer algorithms for fluid/structure interaction problems with non-matching discrete interfaces: Momentum and energy conservation, optimal discretization and application to

aeroelasticity, Computer Methods in Applied Mechanics and Engineering 157 (1998) 95–114.

[60] A. de Boer, A. van Zuijlen, H. Bijl, Review of coupling methods for non-matching meshes, Computer Methods in Applied Mechanics and Engineering 196 (2007) 1515–1525.

[61] J. Blazek, Computational Fluid Dynamics: Principles and Applications, 1st Edition, Elsevier Science, Oxford, 2001.

[62] G. Karypis, V. Kumar, A fast and high quality multilevel scheme for partitioning irregular graphs, SIAM Journal on Scientific Computing 20 (1) (1999) 359–392.

[63] C. Förster, W. A. Wall, E. Ramm, Artificial added mass instabilities in sequential staggered coupling of nonlinear structures and incompressible viscous flows, Computer Methods in Applied Mechanics and Engineering 196 (2007) 1278–1293.

[64] W. Wall, Fluid-struktur-interaktion mit stabilisierten finiten elementen, Ph.D. thesis, Universitat Stuttgart (1999).